JOURNAL OF MATERIALS SCIENCE 27 (1992) 3487–3496

# Mechanisms of phase transformations during laser treatment of grey cast iron

N. ZÁRUBOVÁ, V. KRAUS, J. ČERMÁK
*Institute of Physics, Czechoslovak Academy of Sciences, Na Slovance 2, 180 40 Prague 8, Czechoslovakia*

Pearlitic grey cast iron was surface melted using a 500 W CW $CO_2$ laser at travel speeds 0.5–100 cm $s^{-1}$. Detailed structural analysis of the laser modified layer was performed by optical and scanning electron microscopy (SEM), and microhardness depth profiles were measured. Temperature distribution was calculated from a three dimensional moving point source model, taking only the heat transfer into account. From the structural details observed in the austenitized zone some conclusions on the mechanism and kinetics of the pearlite austenite transformation at high heating rates were drawn. The melted zone consisted of primary austenite and ledeburite. At lower scanning speeds the structure was dendritic, at higher scanning speeds transition to dendritic-cellular structure was observed. From the secondary dendrite arm spacings the cooling rate during solidification was estimated as a function of the depth. Some discrepancies were found between our measurements and the literature data as well as predictions by the simple model neglecting convection in the melt.

## 1. Introduction

An effective control of the laser surface treatment necessitates good understanding of processes occurring at very fast heating and cooling rates. It demands an adequate mathematical description of the thermal cycle, as well as a detailed analysis of the resulting microstructure. The microstructure is, on the one hand, decisive of the final properties of the modified layer. On the other hand, it can yield valuable information on quantities which cannot be measured directly, e.g. the cooling and solidification rates or location of some transformation temperatures ($A_1$, $A_3$, solidus, liquidus), and these quantities can, in turn, verify the mathematical model used.

Laser surface treatment of cast iron has been investigated rather extensively during the last two decades [1–25]. These efforts have concentrated on several problems. The track geometry and microstructure have been treated more or less extensively by all authors. The surface topography and defects, such as pores and cracks, were discussed already in the oldest papers in this field, and still represent a serious problem in laser melting of cast iron [1–4, 10–13, 15, 18, 24]. Bergmann and co-workers [10, 12] and Fouquet and Szmatula [17] claim to have optimized the surface remelting of cast iron so that crack- and pore-free layers with a smooth surface could be produced. As far as the properties of the laser modified layers are concerned, besides the commonly measured microhardness, the wear properties [4, 7–9, 11, 16, 18–21], fatigue [7–9, 11, 12] and corrosion [6, 9] have been investigated.

Though remelting of grey cast iron probably represents one of the oldest applications of laser technologies in metallurgy (the paper by Davydov *et al.* [1] was published as early as 1969), the mechanisms of structural changes during heating and cooling have yet not been fully explained. The aim of this study is to specify in detail the microstructure within the laser modified region, and to give an explanation of some observed phenomena. In particular, the mechanism of pearlite → austenite transformation is discussed, and some quantitative results within the melted zone which contradict the literature data are emphasized.

## 2. Experimental procedure

The material used for experiments was grey cast iron of a composition (in wt%): 3.35 C, 2.0 Si, 0.4 Mn. The starting microstructure consisted of pearlite and medium sized flake graphite. The specimens $10 \times 20 \times 40$ $mm^3$ in ground state were surface melted using a 500 W CW $CO_2$ laser working approximately in $TEM_{00}$ mode. Two laser equipments were used, an Everlase (specimen series I) and a Ferranti (specimen series II). The specimens were located in the focus of a 6.25 mm lens, where the beam diameter was estimated to be roughly 0.2 mm. Corresponding incident power density was about $10^6$ W $cm^{-2}$. The samples, under argon shielding, were traversed relative to the beam at scanning speeds, $v$, varying from 0.5–100 cm $s^{-1}$. The results described refer to single tracks only.

After laser treatment the specimens were sectioned, polished and etched in 5% nital. Microstructural investigations by optical and scanning electron microscopy were carried out mainly on transverse (cross) sections, partly on longitudinal sections perpendicular to the specimen surface. Observations of as-laser

0022-2461

treated material were supplemented in some cases by observations on specimen sections given a subsequent heat treatment for 2 h at 250, 350 or 450 °C, which permitted better identification of some structural components. Metallurgical investigations were correlated with changes of the Vickers microhardness measured with a load of 50 g.

## 3. Mathematical model of the heat transfer

Correct interpretation of the observed structural effects requires an appropriate quantitative description of the temperature distribution. The corresponding mathematical model may be very involved, however, the uncertainty in important constants entering the computations, namely the reflectivity of the samples and their thermal conductivity and diffusivity, did not justify exact and time consuming calculations. Instead, a simplified model was applied of a point source moving at a constant velocity on the surface of the sample taken as the infinite half-space. All physical characteristics were considered to be temperature independent. The stationary solution for this case

$$T = \frac{P}{2\pi r K}\exp\left[-\frac{v(r-x)}{2\varkappa}\right] \qquad (1)$$

as indicated in [26], proved to be satisfactory for all general considerations ($T$ is the temperature at $(x, y, z)$; $P$ is the effective laser power; $r = (x^2 + y^2 + z^2)^{0.5}$ is the radius vector of the point of observation; $K$ is the thermal conductivity; $\varkappa$ is the thermal diffusivity; $v$ is the scanning velocity). Numerical results for $T$ as a function of $v$ were applied in comparing theoretical and experimental temperature profiles. Equation 1 was also used for estimating the heating and cooling rates during the thermal cycle.

## 4. Experimental results

### 4.1. Track geometry

Typical examples of track cross-sections, with well visible melted and austenitized zones, are presented in Fig. 1. The size and shape of the laser modified regions depend strongly on the interaction time. For the lowest scanning speeds the cross-sections are half circles whereas for higher scanning speeds deep, U or V-shaped tracks were observed. In Fig. 2a,b the depth, $d$, and the area, $A$, of the melted and austenitized zones are plotted in dependence of the scanning speed, $v$. The values of $d$ obtained from samples irradiated with different lasers (series I and II) are different, especially at small $v$. On the other hand, the $A$ values, i.e. the melted and the austenitized volumes, are nearly identical for both series indicating that about the same amount of energy was absorbed in both cases.

Calculations of the track size on the basis of Equation 1 were made for the absorbed power 350 W (70% absorptivity), $K = 0.293\ \mathrm{W\,cm^{-1}\,K^{-1}}$, $\varkappa = 0.064\ \mathrm{cm^2\,s^{-1}}$, melting temperature was 1150 °C, and the austenitizing temperature (for reasons explained in Section 5.1) was 900 °C ($\simeq A_3$). As it is apparent from Fig. 2b, the simple model of moving point source describes fairly well the austenitized volume, and for $v \leqq 32\ \mathrm{cm\,s^{-1}}$ also the melted volume. At higher speeds the laser modified region diminishes with increasing $v$ more rapidly than predicted by the model. The reason is undoubtedly high reflectivity of the ground surface. The material in advance of the beam is pre-heated and, thus, its absorptivity enhanced. According to [25] this effect is negligible if the interaction time, $t_i < \rho^2/4\varkappa$ ($\rho$ is the beam radius), which is the case of $v > 32\ \mathrm{cm\,s^{-1}}$ in our experiments. Consequently, a relatively large portion of the interaction time is spent heating the surface to the melting point so that the effective time for melting is, in fact, shorter.

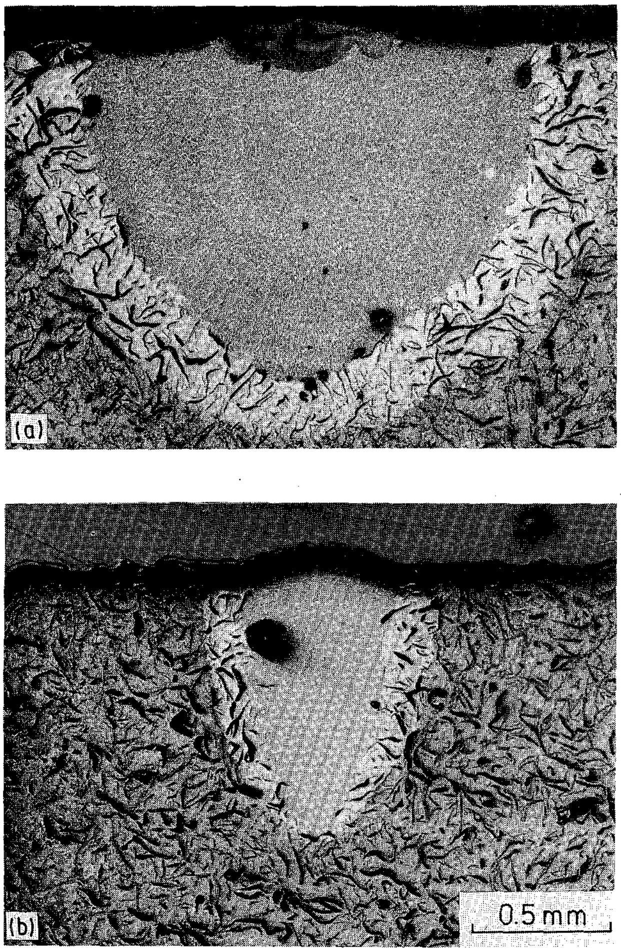

*Figure 1* Cross-sectional views of laser treated samples for scanning speeds: (a) $v = 0.5$ and (b) $v = 4.4\ \mathrm{cm\,s^{-1}}$.

Regarding the shape of the tracks, it seems reasonable to use the model for estimations only for the lowest scanning speeds where the track cross-sections correspond at least approximately to the theoretically predicted half circles.

### 4.2. Structural examinations

#### *4.2.1. The austenitized zone*

Demarcation in the structure between the austenitized zone (AZ) and the parent metal, as well as between the AZ and the melted zone (MZ) is quite sharp. Both boundaries are, however, irregular, particularly due to the graphite lamellae which represent bodies with different thermal properties and distort the temperature field [27].

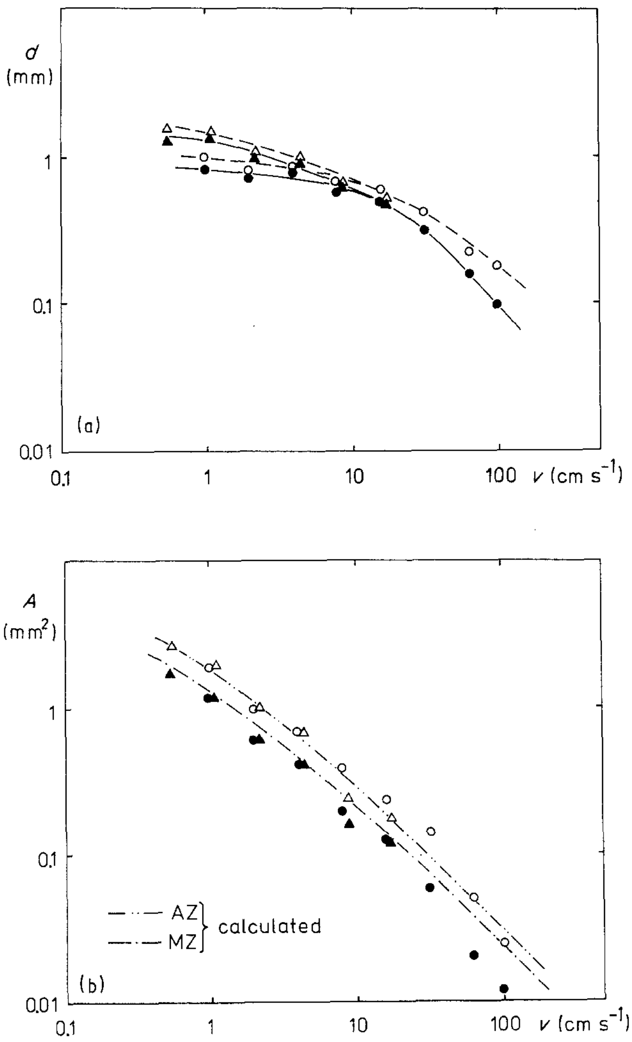

*Figure 2* Depth (a) and area (b) of the austenitized and melted zones as functions of the scanning speed: Specimen series I; (○) AZ and (●) MZ; specimen series II; (△) AZ and (▲) MZ.

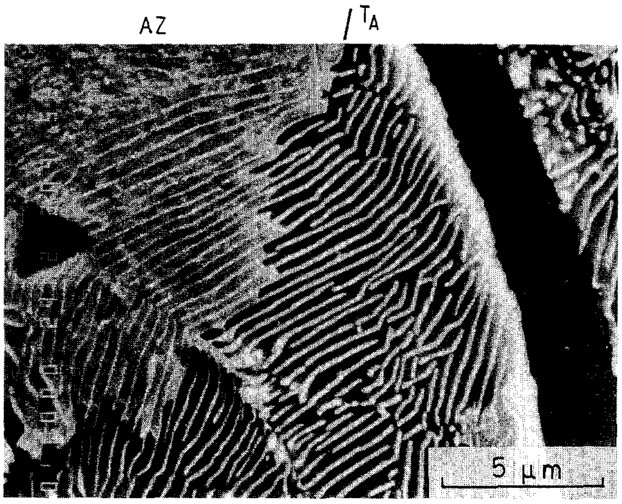

*Figure 3* Undissolved cementite lamellae near the boundary (line $T_A$) between the austenitized zone and the original material.

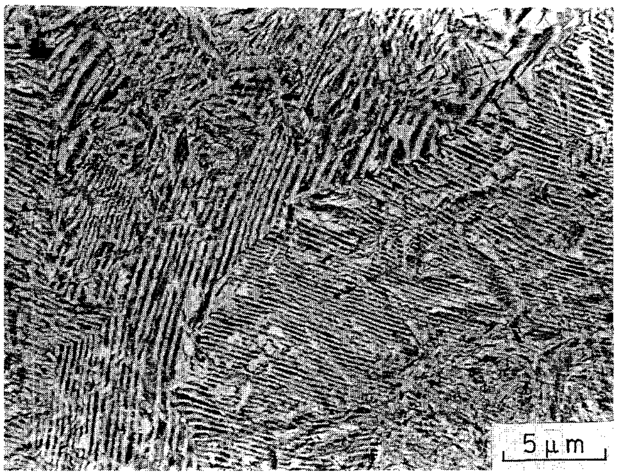

*Figure 4* Chemical heterogeneity (pearlite ghosts) in the austenitized zone. The sample was subsequently annealed for 2 h at 250 °C.

The basic structure of the AZ consists of martensite with retained austenite, and undissolved graphite. A remarkable structural component is, however, fine stripping (Figs 3 and 4) resembling the cementite lamellae, which is observable in the whole austenitized zone, sometimes up to the solidus. The heterogeneity is of two types. Close to the outer boundary of the AZ, where the peak temperature was relatively low and the thermal cycle short, the cementite plates continue from the original pearlite grains into the austenitized matrix (Fig. 3). The thickness of the plates often remains apparently unchanged. In this case, the strips represent a phase heterogeneity—residual cementite lamellae which remained undissolved during the heating period. Far from the outer boundary the cementite lamellae disappear. Nevertheless, traces of the original pearlitic structure are still apparent (Fig. 4). They are due to a chemical heterogeneity—enhanced carbon content in the places where the cementite plates have just dissolved (pearlite ghosts [28]). Both types of heterogeneities can be distinguished from the morphology of the matrix. In the case of the phase heterogeneity (residual cementite) martensite is very fine and the size of the martensite crystals is limited by the two adjoining cementite plates. In the case of the chemical heterogeneity the martensite needles intersect several ghosts and become stripped after etching (Fig. 4). This stripping is already visible in the as-laser treated state and becomes much more pronounced after subsequent heat treatment.

Going from the periphery to the zone interior the content of dissolved carbon in the austenite increases as a result of increasing peak temperature and a prolonged heating period. Consequently, changes in the morphology of martensite and in the content of retained austenite are observed. Whereas close to the outer boundary of the AZ the martensite is very fine and featureless, in the zone interior the martensite needles become larger and more pronounced (see Figs 5 and 6). Close to the solidus the martensite needles with typical midribs form chains often giving rise to microcracks (Fig. 6), which is typical of twin martensite with high carbon content. The amount of retained austenite increases going from the outer boundary towards the track interior. Close to the solidus there is a narrow region—about 10 μm thick—which is almost fully austenite, with individual martensite needles (Fig. 5). It indicates that the $M_s$ temperature decreased to room temperature in this region, undoubtedly as a result of high carbon enrichment from the melt.

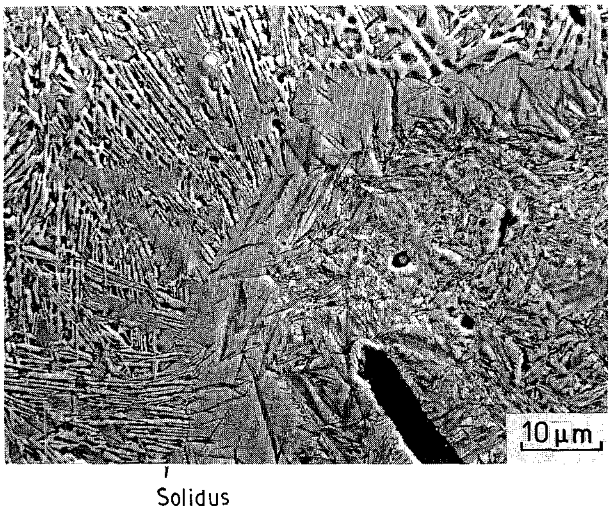

*Figure 5* Boundary between the austenitized and melted zones with well visible austenite region beneath the solidus.

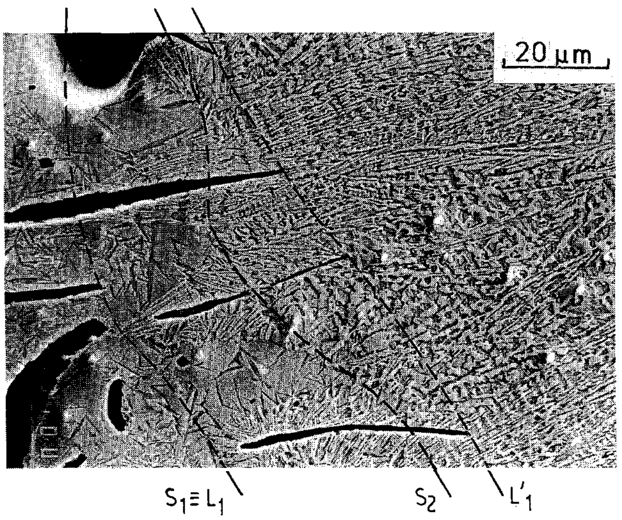

*Figure 7* Detail of the boundary between the austenitized and melted zones.

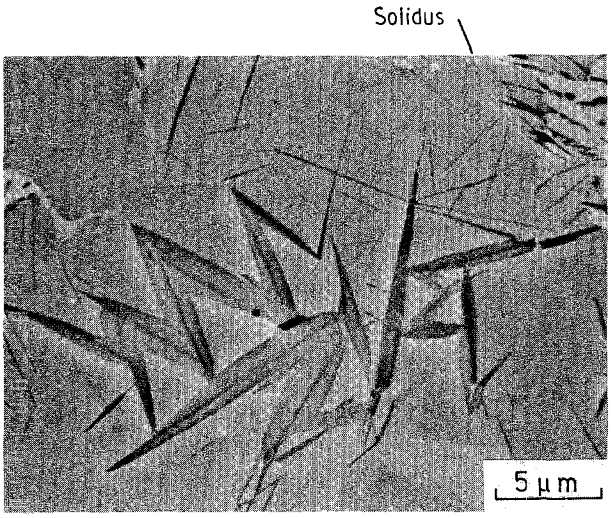

*Figure 6* Typical martensite chains near the austenitized zone/melted zone interface.

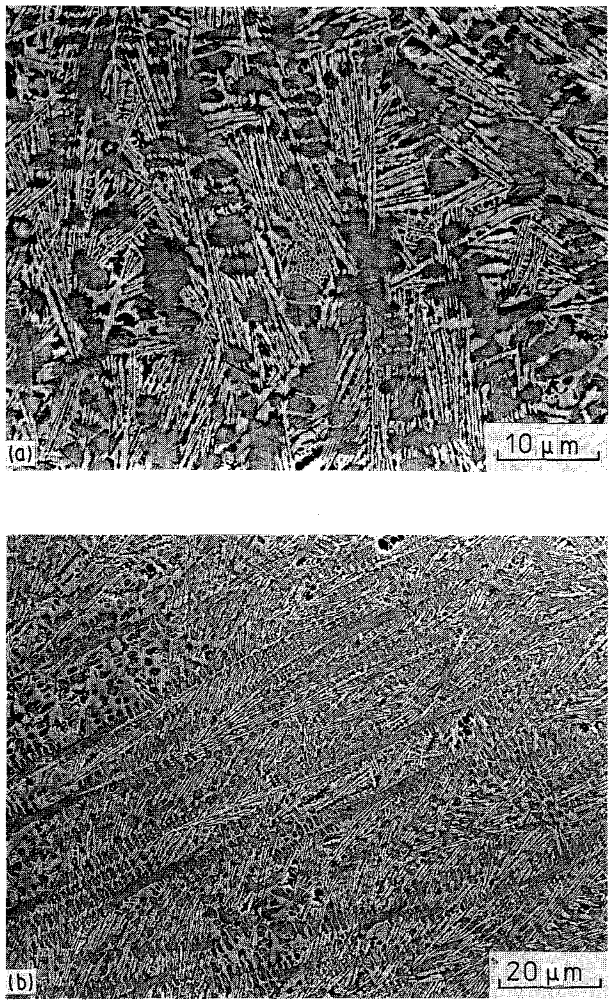

*Figure 8* Dendritic structure of the melted zone at lower scanning speeds: (a) $v = 2.2$, cross-section, and (b) $v = 4$ cm s$^{-1}$, longitudinal section.

### 4.2.2. The melted zone

The boundary between the AZ and MZ is complicated as illustrated by Fig. 7. Melting occurs first in the close vicinity of the graphite flakes where the austenitized matrix has been carbon enriched and the melting point locally lowered. As a result melt protrudes deeply into the AZ (line $S_1 \equiv L_1$) and, after resolidification, fine ledeburite is observed at the places adjacent to the graphite lamellae. At places most remote from the graphite flakes fusion starts at temperature, $S_2$. The graphite flakes completely dissolve above temperature $L'_1$.

The structure of the melted zone consists of partially transformed primary austenite and ledeburite. At lower scanning speeds, $v \leqq 32$ cm s$^{-1}$, the structure is dendritic with a pronounced texture (Fig. 8a and b). In the cross-sections, dendrites of primary austenite are oriented preferentially towards the track centre, in the longitudinal sections there is a tendency for dendrites to approximately follow a trajectory which is at any point perpendicular to the advancing crystallization front. The carbon content in the primary austenite is high, as indicated by low (some per cent) amount of martensite in the as-laser treated samples (Fig. 9a). At higher scanning speeds, $v > 32$ cm s$^{-1}$, dendritic-cellular structure, again with a pronounced texture, is

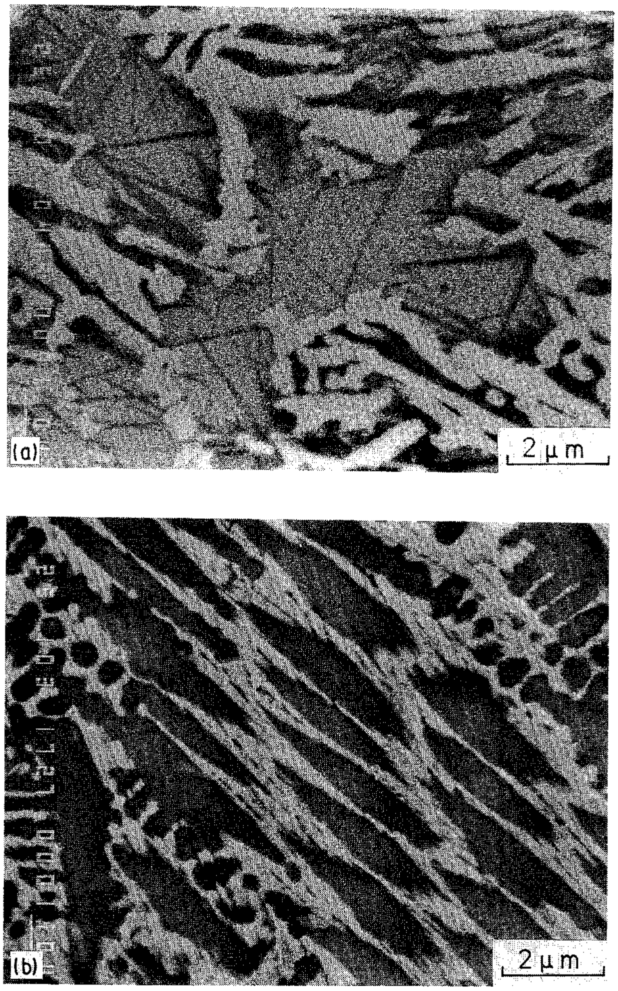

*Figure 9* Details of the structure in the melted zone, cross-sections: (a) $v = 0.5$ and (b) $v = 100\,\mathrm{cm\,s^{-1}}$.

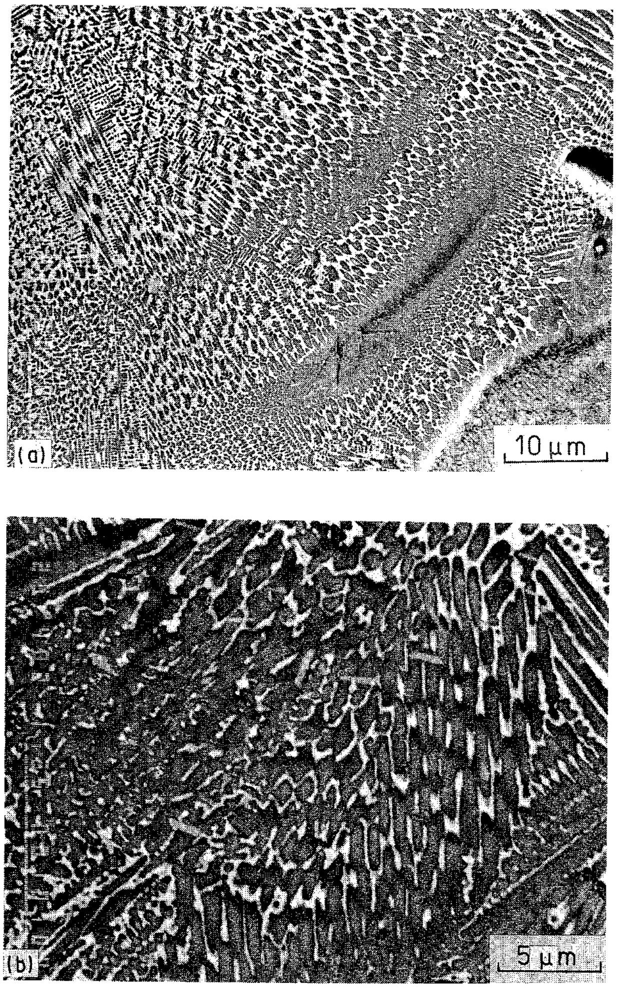

*Figure 10* Cellular-dendritic structure at the bottom of the melted zone observed at higher scanning speeds, cross-section: (a) $v = 32$ and (b) $v = 100\,\mathrm{cm\,s^{-1}}$.

observed (Figs 9b and 10a,b).The microstructure consists only of cementite and austenite, no martensite needles can be distinguished. This is most probably due to high carbon content in the austenite, which suppresses the martensitic transformation (see also [17]).

The secondary dendrite arm spacings, $\lambda$, are usually taken as a quantitative measure of the cooling rate, $\dot{T}$. Fig. 11 summarizes results of our measurements of $\lambda$ for scanning speeds up to $32\,\mathrm{cm\,s^{-1}}$ (region of well developed dendrite structure). The spacings $\lambda$ were measured on metallographic sections at various depths in the melted zone. The right hand scale in Fig. 11 gives corresponding cooling rates calculated from the empirical relation $\lambda \times \dot{T}^{a} = c$ derived by Matyja *et al.* [29]. For the empirical constants the values $a = 0.264$, $c = 18.2$ published for Fe–2%Si–3%C by Kurobe *et al.* [30] were taken. Though the magnitude of the cooling rate is not very reliable because of the uncertainty in the constants $a$ and $c$, the relative values should be correct. It is apparent from Fig. 11 that for all scanning speeds $\lambda$ decreases with increasing depth in the melted zone. It means at the same time an increasing cooling rate with augmenting depth under the surface.

### 4.3. Microhardness

The depth profiles of microhardness, presented for two scanning speeds in Fig. 12, are very similar to those published in papers [4, 14, 17]. The hardness of untreated material was about 250 HV. Changes found after laser treatment correspond very well to the structural changes within the austenitized and melted zones. In the AZ microhardness rapidly increases due to high content of martensite reaching a maximum of $\simeq 1000$ HV. This maximum is obviously a consequence of the fact that the content of dissolved carbon in the austenite increases with decreasing depth, $z$, in the AZ (see Section 4.2.1.). This increasing carbon content results, on the one hand, in increasing hardness of martensite (see e.g. the measurements in [31]), and on the other hand, however, in an increasing amount of soft retained austenite. In the narrow, almost fully austenite region close to the solidus the hardness is as low as 500 HV. In the melted zone, with increasing content of ledeburite, the hardness increases again very rapidly to about 1100 HV for $v = 0.5\,\mathrm{cm\,s^{-1}}$, and to a lower value, about 700 HV, for $v = 17.6\,\mathrm{cm\,s^{-1}}$. Towards the specimen surface the hardness decreases slightly, probably due to higher amounts of primary austenite. With increasing

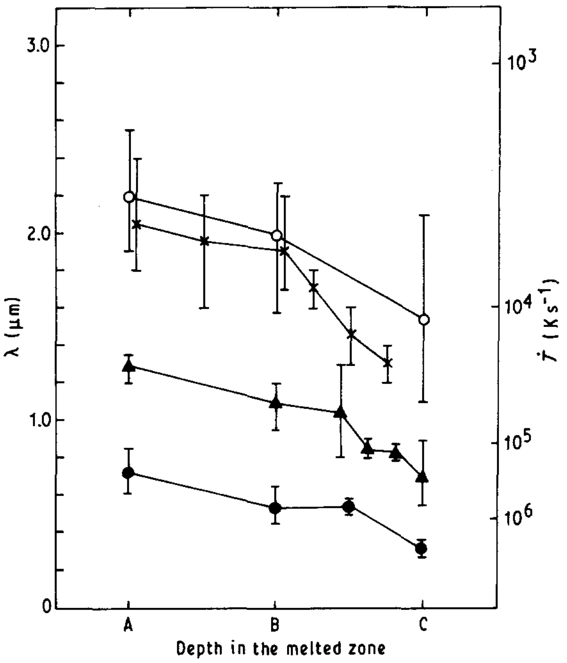

*Figure 11* Secondary dendrite arm spacing, λ, as a function of the depth in the melted zone for various scanning speeds. Coordinates A, B, C correspond approximately to the top, centre and bottom of the zone, respectively. The right-hand scale indicates the calculated cooling rate, $\dot{T}$: $v$ = (○) 1; (×) 2; (▲) 8 and (●) 32 cm s$^{-1}$.

scanning speed the hardness of the MZ systematically falls to about 500 HV at $v$ = 100 cm s$^{-1}$. This fall is most probably due to a decreasing amount of martensite (see Section 4.2.2.), and perhaps also of cementite, in the remelted structure. However, quantitative measurements of the cementite content have not been made.

## 5. Discussion

### 5.1. Mechanisms of pearlite–austenite transformation

It is well known that at moderate heating rates pearlite → austenite transformation occurs by the reaction $Fe_\alpha(C) + Fe_3C \rightarrow Fe_\gamma(C)$ after the $A_{c_1}$ temperature has been exceeded. As described by Roberts and Mehl [28] austenite forms by a process of nucleation and growth, and the transformation rate depends on the rate of dissolution of carbide and rate of migration of carbon atoms in the austenite. The kinetics of this transformation on continuous heating may be described by means of a C.H.T. (continuous heating – transformation) diagram as schematically shown in Fig. 13b for heating rates $U < U'_L$. The transformation takes place in a temperature interval laying between $A_{c_1}$ and $A_{c_3}$. As soon as the transformation has been completed, the pearlite disappears as a structural constituent. The austenite is, however, not homogeneous and residual carbon particles remain in the austenite matrix. They dissolve on continued heating but carbon concentration gradients still exist (pearlite ghosts – region $\gamma^*$ in Fig. 13b). During further heating carbon redistribution in austenite occurs and, eventually, homogeneous austenite results (region $\gamma$ in Fig. 13b).

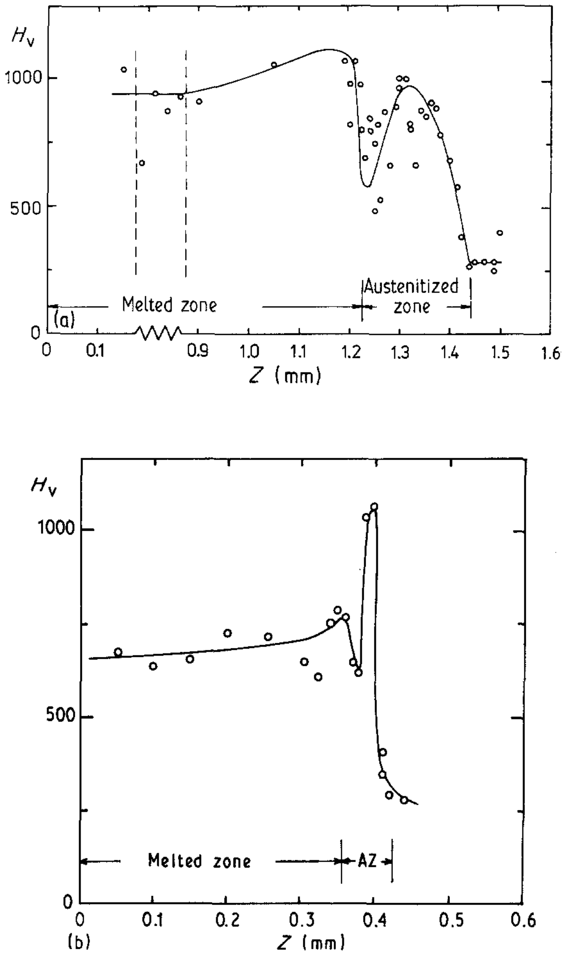

*Figure 12* Depth profiles of microhardness: (a) $v = 0.5$ and (b) $v = 17.6$ cm s$^{-1}$.

Formation of austenite by heterogeneous nucleation and diffusion controlled grain growth takes place when heating the specimen without appreciable temperature gradients, e.g. during conventional heat treatments or surface quenching. Laser heat treatment, on the other hand, is accompanied by large temperature gradients which can modify the mechanism of the pearlite → austenite transformation.

Austenitization during laser heating has been treated by several authors [31–36]. Ashby and Easterling [31] investigated laser transformation hardening in hypo-eutectoid steels. They combined a solution for the temperature field with kinetic equations for the conversion of pearlite and ferrite to austenite, and for the subsequent transformation of austenite to martensite. The pearlite → austenite transformation is supposed to occur above the $A_1$ temperature by dissolution of cementite lamellae, and a certain superheating is predicted.

A detailed study of the mechanism of the pearlite → austenite transformation based on metallurgical investigations as well as theoretical considerations has been published by Lepski and co-workers [32–34]. As discussed [32–34] austenitization during laser heat treatment can occur by two competing processes: by heterogeneous nucleation and growth, similarly to the conventional heat treatments, or by diffusion controlled propagation of the $\alpha/\gamma$ interface which is in the steady state running in front of the hot ($T > A_3$) zone

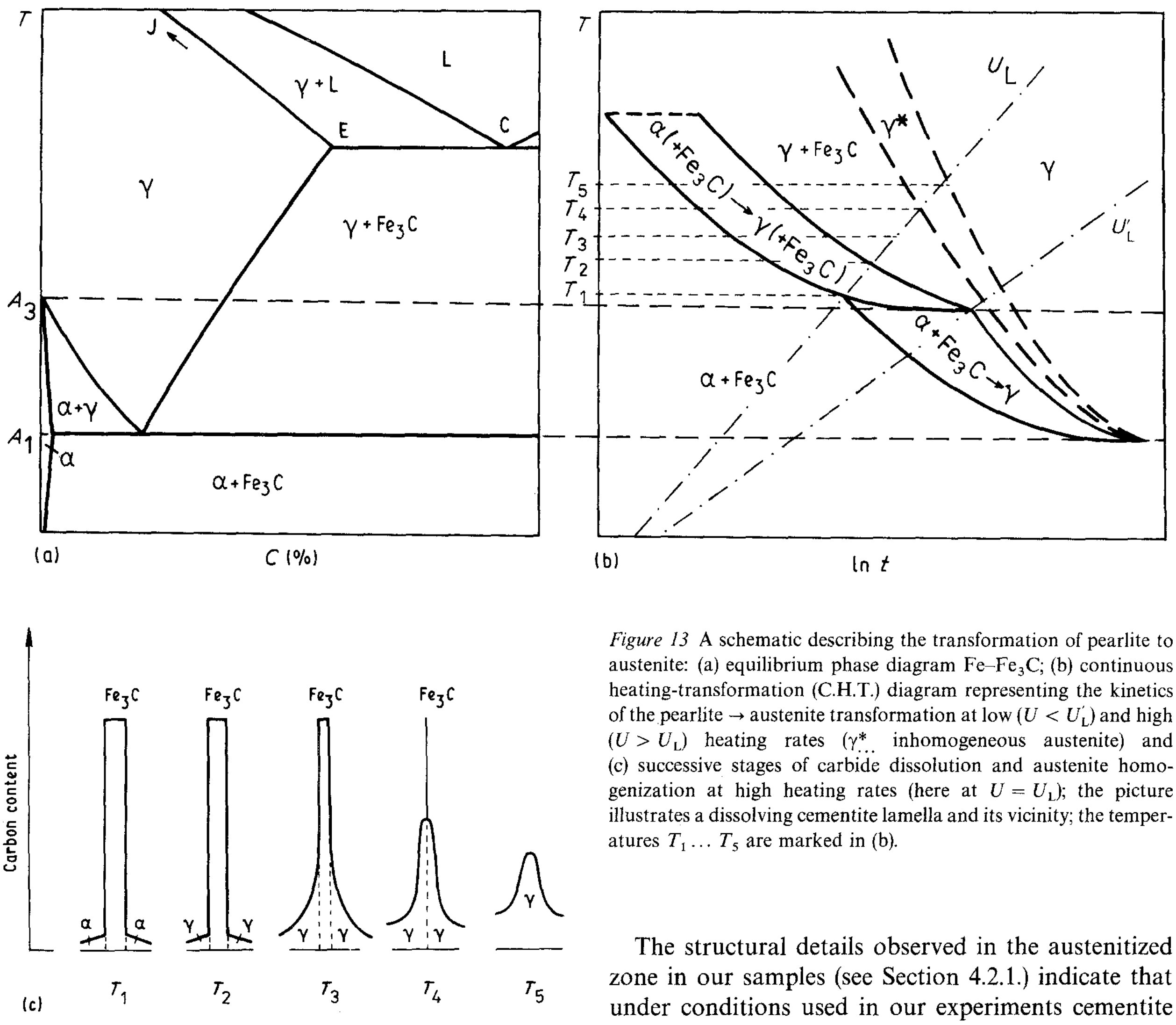

*Figure 13* A schematic describing the transformation of pearlite to austenite: (a) equilibrium phase diagram Fe–$Fe_3C$; (b) continuous heating-transformation (C.H.T.) diagram representing the kinetics of the pearlite → austenite transformation at low ($U < U'_L$) and high ($U > U_L$) heating rates ($\gamma^*_{..}$ inhomogeneous austenite) and (c) successive stages of carbide dissolution and austenite homogenization at high heating rates (here at $U = U_L$); the picture illustrates a dissolving cementite lamella and its vicinity; the temperatures $T_1 \ldots T_5$ are marked in (b).

through the surface layer. At this interface ferrite undergoes diffusion controlled transformation into austenite without local nucleation. Which of the two mechanisms becomes dominant depends on the heating rate (i.e. on the front propagation speed and the temperature gradient). Nucleation of austenite may occur only if the heating rate is low enough so that the time during which the material ahead of the $\alpha/\gamma$ interface has a temperature between $A_1$ and $A_3$ exceeds the incubation time for nucleation. At higher heating rates the front propagation mechanism is dominant. This mechanism was well demonstrated in papers [32–34] and it was shown that the austenitization temperature $T_A$ (i.e. the lowest temperature at which $\alpha \rightarrow \gamma$ transformation can occur) increases with increasing laser scanning speed.

Under the experimental conditions used in papers [31–34] the heating rate during the thermal cycle was obviously relatively low and the pearlite → austenite transformation occurred by the classical mechanism $Fe_\alpha(C) + Fe_3C \rightarrow Fe_\gamma(C)$ between the $A_1$ and $A_3$ temperatures. This mechanism necessitates sufficiently intense diffusion flux of carbon so that the rate controlling process is dissolution of the carbide and diffusion of carbon. The kinetics of this transformation is expressed schematically by the lower part of the C.H.T. diagram in Fig. 13b (for $U < U'_L$).

The structural details observed in the austenitized zone in our samples (see Section 4.2.1.) indicate that under conditions used in our experiments cementite did not participate in the pearlite → austenite transformation, or its participation was very limited. It is well documented by the fact that at the lowest scanning speeds undissolved cementite lamellae are observed at the outer boundary of the AZ. Thus, the austenitization temperature, $T_A$, must have been shifted to the $A_3$ temperature and the transformation took place completely, or at least predominantly, by the direct mechanism $Fe_\alpha(+ Fe_3C) \rightarrow Fe_\gamma(+ Fe_3C)$ with subsequent dissolution of cementite. The same effect was observed on plain carbon steel by Luft *et al.* [33] who reported shifting of the austenitization temperature, $T_A$, to the $A_3$ temperature for their highest laser scanning speeds. Similarly, Bradley and Kim [35, 36] observed in a laser hardened Cr-alloyed steel that below a fully austenitized zone there was a zone where remnants of the original pearlite structure were still visible: transformation of the ferritic component of the pearlite proceeded between the cementite plates while the cementite itself remained undissolved.

The kinetics of austenitization at high heating rates is schematically depicted by the C.H.T. diagram in the upper part of Fig. 13b. Whereas for heating rates $U < U'_L$ the transformation occurs *via* carbide dissolution and is completely controlled by diffusion of carbon, at $U > U_L$ merely direct transformation $Fe_\alpha \rightarrow Fe_\gamma$ takes place. Since this transformation is a nucleation and growth process, as clearly demonstrated for laser treated carbon steel with pearlitic structure in [33], it will occur again in a temperature interval.

The limiting heating rates $U_L$, $U_L'$ which separate the two different mechanisms of the $\alpha \rightarrow \gamma$ transformation will depend on both chemical composition and morphology of the original structure. For example, Bradley and Kim [35, 36] proved the retarding effect of Mn and Cr on solubility of cementite and, hence, on the kinetics of the $\alpha \rightarrow \gamma$ transformation during laser heating. A similar analysis in our experimental conditions seems useful. An estimation based on the point source model yields for $v = 1\ \mathrm{cm\,s^{-1}}$ the heating rate at the bottom of the AZ about $3 \times 10^3\ \mathrm{K\,s^{-1}}$. The limiting rates $U_L$, $U_L'$ are obviously below this value in our material. The characteristic diffusion distance, $s$, can be estimated from the formula [31, 35]

$$s^2 = 2D_0 \int_{t_1}^{t_2} \exp[-Q/RT(t)]\,dt \qquad (2)$$

where R is the gas constant, $T(t)$ is the temperature–time profile, and $t_1$, $t_2$ are the times when the $A_1$ temperature is reached upon heating and cooling, respectively. For the diffusion of carbon in austenite ($Q = 1.35 \times 10^5\ \mathrm{J\,mol^{-1}}$ and $D_0 = 1 \times 10^{-5}\ \mathrm{m^2\,s^{-1}}$ [31]) we get at the bottom of the AZ, where the maximum temperature was $A_3 \simeq 900\,^\circ\mathrm{C}$, the distance $s \simeq 0.14\ \mu\mathrm{m}$. The interlamellar spacings are typically 0.3 μm, and, thus, the heating cycle would be sufficient to fully austenitize the pearlite if the carbon diffusion in austenite were the rate controlling process. The undissolved cementite lamellae within the AZ indicate, however, a slower transformation kinetics, undoubtedly because Mn stabilizes the carbide [37] and Si concentrated in ferrite reduces the solubility of carbon in Fe [38, 33].

Fig. 13c illustrates dissolution of the cementite plates for $U = U_L$, after the $\alpha \rightarrow \gamma$ transformation has been completed. In the figure carbide dissolution and austenite homogenization is schematically shown for several temperatures marked in Fig. 13b. At $T_1$ the $\mathrm{Fe}_\alpha \rightarrow \mathrm{Fe}_\gamma$ transformation starts, at $T_2$ the transformation is finished. At that moment undissolved cementite lamellae and low-carbon austenite matrix coexist. With increasing temperature the carbide rapidly dissolves giving rise to a carbon concentration gradient in the austenite ($T_3$). Up to temperature $T_4$ phase heterogeneity described in Section 4.2.1. exists. Near $T_4$ carbide begins to disappear as a structural component but chemical heterogeneity, visible after quenching as pearlite ghosts, remains ($T_5$). After cooling various stages of the dissolution process are visible within the AZ depending on the local peak temperature and duration of the thermal cycle. In the micrographs faint pearlite ghosts are sometimes visible even at places adjacent to the melted zone indicating that heterogeneities in the carbon distribution persist up to the solidus. As the carbon content in the austenite depends on the peak temperature and the duration of the thermal cycle, it should increase in the direction from the outer boundary of AZ to the solidus. This seems to be fully proved by the changes in the morphology of martensite and in the content of retained austenite observed within AZ. Also the microhardness depth profiles correspond very well to this change.

## 5.2. The fusion region

From the form of the outer boundary of the MZ it is evident that melting occurred by two different mechanisms, depending on the distance from the graphite lamellae. At the graphite/austenite interface it proceeded by reaction of these phases and the resulting melt was of eutectic composition. Because of high rate of this reaction a negligible overheating may be expected so that solidus, $S_1$, and liquidus, $L_1$, are identical and correspond to the eutectic temperature $\simeq 1150\,^\circ\mathrm{C}$ (line EC in Fig. 13a). The line $S_1 \equiv L_1$ in Fig. 7 represents the lowest temperature of fusion.

With increasing distance from the graphite lamellae solidus moves along the line EJ in the equilibrium diagram (Fig. 13a). The solidus at the places most remote from the graphite lamellae is represented by the line $S_2$ in Fig. 7 (the corresponding liquidus cannot be reliably distinguished in the microstructure). If we use the point source model, the distance between the isotherms $S_1$ and $S_2$ (typically 40 μm) corresponds to a temperature difference of about 75 K. The temperature $L_1'$ in Fig. 7 represents the macroscale liquidus above which relatively homogeneous melt exists.

## 5.3. Structure of the melted zone; cooling rate during solidification

It is commonly accepted that the character of the microstructure is controlled by the temperature gradient to solidification rate ratio, $G/V_s$, whereas the scale of the microstructure is determined by the cooling rate, $\dot{T} = GV_s$. Increasing the $G/V_s$ ratio causes a change from dendritic to cellular growth. Increasing the cooling rate gives rise to finer structure [39]. Let us compare the experimental data and the heat transfer model used in this paper from this point of view.

According to the heat transfer analysis the cooling rate should remain approximately constant going along any isotherm (and, thus, along the solidification front as well) from the surface into the MZ depth. Near the bottom of the MZ the cooling rate should rapidly decrease. Similar dependence of the cooling rate at the melt/solid interface on the depth was derived from one dimensional point source model by Breinan and Kear [39], and experimentally confirmed in [3, 5, 40]. On the contrary, Fig. 11 clearly shows an increase of the cooling rate as the bottom of the MZ is approached.

Similarly, according to the point source model the $G/V_s$ ratio should decrease with increasing scanning speed: for $T = 1270\,^\circ\mathrm{C}$ (the equilibrium liquidus temperature for Fe–3.35%C) and variables $P$, $K$ and $\varkappa$ (the same as used in Section 4.1.), in the central part of the melted zone, $G/V_s \simeq 10^4\ \mathrm{K\,s\,cm^{-2}}$ for $v = 1\ \mathrm{cm\,s^{-1}}$, and $G/V_s \simeq 10^3\ \mathrm{K\,s\,cm^{-2}}$ for $v = 100\ \mathrm{cm\,s^{-1}}$. This decrease of $G/V_s$ contradicts the observed transition from the dendritic to cellular structure when going from the lower to the higher scanning speeds.

The cause of these disproportions is most probably convection in the melt which has been neglected in simple models. Since the melted zones were rather deep, significant convection may be expected [41]. According to [42] the velocity of the flow can be of one or two orders of magnitude higher than the scanning speed so that the temperature distribution in the melt pool may be considerably changed.

## 6. Conclusions

Microstructural changes in laser melted grey cast iron have been investigated. The main results are as follows:

1. Under irradiation conditions used in our experiments (incident power density $\simeq 10^6$ W cm$^{-2}$) surface melting occurred at scanning speeds up to 100 cm s$^{-1}$. The track size may be well described by a simple model of moving point source respecting only the heat transfer.

2. The austenitized zone consisted of martensite, the retained austenite and undissolved graphite. The remnants of cementite lamellae and pearlite ghosts observed within the austenitized zone indicate that at high heating rates the pearlite → austenite transformation takes place by the direct mechanism $Fe_\alpha(+Fe_3C) \rightarrow Fe_\gamma(+Fe_3C)$ with subsequent dissolution of cementite. A new type of C.H.T. diagram was proposed for $\alpha \rightarrow \gamma$ transformation and homogenization of the austenite.

3. The structure of the melted zone was formed by partly transformed austenite and ledeburite. At lower scanning speeds dendritic structure was observed. From the secondary dendrite arm spacings the cooling rate during solidification was estimated. For all scanning speeds the cooling rate was the highest at the bottom of the melted zone and the lowest near the surface, in contradiction with simple calculations (considering the heat transfer only) of the cooling rates along isotherms in dependence on the depth, and with some literature data.

4. At high scanning speeds transition to cellular structure occurred. This observation contradicts the calculations of the temperature gradient to solidification rate ratio, $G/V_s$, as a function of the scanning speed, and, similarly to the cooling rate, seems to be anomalous as well. The cause of these discrepancies is most probably convection in the melt, which has been neglected in the model.

5. Microhardness was enhanced by the laser treatment from the value of 250 HV for the untreated material to 500–1100 HV in the melted zone. The microhardness–depth profiles correspond very well to the structural changes observed within the laser modified region.

## Acknowledgements

The authors would like to thank Mrs G. Gardavská for the microhardness measurements, Dr K. Jurek and Mrs M. Šimečková for their help with electron microscopy, and Dr A. Luft (ZFW Dresden) and Dr M. Čerňanský for valuable comments on the manuscript.

## References

1. J. I. DAVYDOV, A. A. ZHUKOV, A. N. KOKORA and M. A. KRISHTAL, *Fiz. i Chim. Obrab. Materialov* (1969) no. 1, 17.
2. A. N. KOKORA, A. A. ZHUKOV and L. Z. EPSHTEIN, *ibid.* (1977) no. 3, 28.
3. V. K. SEDUNOV, V. M. ANDRJACHIN, N. T. CZEKANOVA and V. M. BELOV, *MITOM* (1980) no. 9, 10.
4. D. N. H. TRAFFORD, T. BELL, J. H. P. C. MEGAW and A. S. BRANSDEN, *Metals Technol.* **10** (1983) 69.
5. H. W. BERGMANN, B. L. MORDIKE and H. U. FRITSCH, *Z. Werkstofftech.* **14** (1983) 237.
6. C. H. CHEN, C. J. ALTSTETTER and J. M. RIGSBEE, *Met. Trans.* **15A** (1984) 719.
7. H. W. BERGMANN, B. L. MORDIKE, F. REINKE and J. BETZ, in "Laser — Optoelectronics in Engineering", edited by W. Waidelich (Springer-Verlag, Berlin, 1985) p. 495.
8. H. W. BERGMANN and M. YOUNG, in "Lasers in Manufacturing", edited by M. E. Kimmit (LIM-2, Birmingham, 1985) p. 109.
9. H. W. BERGMANN, in "Laser Surface Treatment of Metals", edited by C. W. Draper and P. Mazzoldi, NATO ASI Series E, No. 115 (Martinus Nijhoff, Dordrecht, 1986) p. 351.
10. B. L. MORDIKE and H. W. BERGMANN, *Mat. Res. Soc. Symp. Proc.* **58** (1986) 3.
11. *Idem, ibid.* **58** (1986) 429.
12. H. W. BERGMANN and G. NEUSE, in "Laser Treatment of Materials", edited by B. L. Mordike (DGM Informationsgesellschaft, Oberursel, 1987) p. 223.
13. A. GILNER, K. WISSENBACH and E. W. KREUTZ, *ibid.* p. 205.
14. *Idem, ibid.* p. 213.
15. R. DEKUMBIS, P. MAGNIN and G. BARBEZAT, *ibid.* p. 195.
16. J. ADAMKA and J. STYK, *ibid.* p. 235.
17. F. FOUQUET and E. SZMATULA, *Mater. Sci. Eng.* **98** (1988) 305.
18. M. BAMBERGER, M. BOAS and O. AKIN, *Z. Metallkde* **79** (1988) 807.
19. W. REITZENSTEIN, D. LEPSKI, A. LUFT and B. BRENNER, in Proceedings of the 3rd Symposium on Heat Treatment "Grundlagen und Anwendung moderner Wärmebehandlungstechnologien für Eisenwerkstoffe", Wissenschaftliche Tagungen der TU Karl-Marx-Stadt 13 (1988) p. 104.
20. A. LUFT, B. BRENNER, W. LÖSCHAU and W. REITZENSTEIN, in Proceedings of the International Symposium on Electron Microscopy in Plasticity and Fracture Research of Materials, edited by U. Messerschmidt, F. Appel, J. Heidenreich and V. Schmidt, Physical Research Vol 14 (Akademie-Verlag Berlin, 1990) p. 97.
21. A. LUFT, B. BRENNER, R. FRANKE and W. REITZENSTEIN, in Proceedings of the Conference "Special Technologies "90", Plzeň (Czechoslovakia), 1990 (Škoda Concern Plzeň, 1990) p. 221.
22. V. KRAUS, N. ZÁRUBOVÁ and J. ČERMÁK, *ibid.* p. 121.
23. *Idem*, in Proceedings of the XIII Conference on Heat Treatment, Vysoké Tatry (Czechoslovakia), 1990 (Dům techniky Bratislava, 1990) p. 56.
24. A. LUFT, W. REITZENSTEIN, N. ZÁRUBOVÁ and J. ČERMÁK, *Schweissen und Schneiden*, **43** (1990) 137.
25. H. W. BERGMANN, *Surf. Eng.* **1** (1985) 137.
26. H. S. CARSLAW and J. C. JAEGER, in "Conduction of Heat in Solids" (Oxford University Press, London, 1978).
27. P. WOLF, J. ČERMÁK and N. ZÁRUBOVÁ, *Kovové materiály*, in press.
28. G. A. ROBERTS and R. F. MEHL, *Trans. ASM* **XXXI** (1943) 613.
29. H. MATYJA, B. C. GIESSEN and N. J. GRANT, *J. Inst. Metals* **96** (1968) 30.

30. J. KUROBE, H. SAKUTA, Y. MIYATA, T. SUZUKI and Y. ICHINOSE, *J. Iron Steel Inst. Jpn* **75** (1989) 1170.
31. M. F. ASHBY and K. E. EASTERLING, *Acta Metall.* **32** (1984) 1935.
32. D. LEPSKI, A. LUFT and W. REITZENSTEIN, in Proceedings of the 5th International Congress on Heat Treatment of Materials, Budapest 1986, Vol. 3 (Scientifique Society of Mechanical Engineers, Budapest, 1986) p. 1560.
33. A. LUFT, D. LEPSKI, B. BRENNER and W. REITZENSTEIN, *Wissenschaftliche Berichte des ZFW Dresden* **36** (1988) 111.
34. D. LEPSKI, A. LUFT and W. REITZENSTEIN, *Opto Elektronik Magazin* **6** (1990) 159.
35. J. R. BRADLEY and S. KIM, *Met. Trans.* **19A** (1988) 2013.
36. *Idem, Scripta Metall.* **23** (1989) 131.
37. R. R. JUDD and H. W. PAXTON, *Trans. AIME* **242** (1968) 206.
38. M. HILLERT, K. NILSSON and L. E. TÖRNDAHL, *J. Iron Steel Inst.* **209** (1971) 49.
39. E. M. BREINAN and B. H. KEAR, in "Laser Materials Processing", edited by M. Bass (North-Holland Publishing Company, 1983) p. 235.
40. E. RAMOUS and R. MENIN, in Proceedings of the 4th International Conference on Rapidly Quenched Metals, Sendai 1981, edited by T. Masumoto and K. Suzuki (The Japan Institute of Metals, Sendai, 1982) p. 189.
41. A. WALKER, D. R. F. WEST and W. M. STEEN, *Metals Technol.* **11** (1984) 399.
42. C. CHAN, J. MAZUMDER and M. M. CHEN, *Met. Trans.* **15A** (1984) 2175.

*Received 18 February*
*and accepted 20 June 1991*